Supporting Information

Coupling Multiphase-Fe and Hierarchical N-doped Nanocarbon as Trifunctional Electrocatalysts by Supramolecular Preorganization of Precursors

Zhixin Zhou,[a] Fei He,[a] Yanfei Shen,[b] Xinghua Chen,[a] Yiran Yang,[a] Songqin Liu,[a] Toshiyuki Mori,[c] and Yuanjian Zhang[a]*

[a.] Jiangsu Engineering Laboratory of Smart Carbon-Rich Materials and Device, Jiangsu Province Hi-Tech Key Laboratory for Bio-Medical Research, School of Chemistry and Chemical Engineering, Southeast University, Nanjing 211189, China. E-mail: Yuanjian.Zhang@seu.edu.cn

[b.] Medical School, Southeast University, Nanjing 210009, China.

[c.] Global Research Center for Environment and Energy Based on Nanomaterials Science (GREEN), National Institute for Materials Sciences (NIMS), 1-1 Namiki, Ibaraki, 305-0044, Japan.

List of Contents

Figure S2. SEM image of BA-TAP.

Figure S3. FT-IR spectra of the BA, TAP, BA-TAP and BA-TAP-Fe.

Figure S4. (a) SEM image of BA-TAP-Fe, and EDX elemental mapping images of (b) C, (c) N, (d) O, and (e) Fe, (f) Cl and (g) corresponding EDX spectrum.

Figure S5. SEM images of BA-TAP-800 (a), BA-Fe-800 (b), TAP-Fe-800 (c) and BA+TAP+Fe-800 (d).

Figure S6. Raman spectra of BA-Fe-800, BA-TAP-800, TAP-Fe-800, BA+TAP-Fe-800, and BA-TAP-Fe-800.

Figure S7. Pore size distribution of BA-TAP-Fe, BA-TAP-Fe-800 and BA+TAP+Fe-800.

Figure S8. CV profiles of BA-TAP-Fe-800.

Figure S9. LSV curves of BA-TAP-Fe-800, BA-TAP-Fe-700 and BA-TAP-Fe-900.

Figure S10. (a) Hydrogen peroxide yield and (b) corresponding electron transfer number of BA-TAP-Fe-800 and Pt/C for ORR.

Figure S11. (a) Chronoamperometric response of BA-TAP-Fe-800 and Pt/C for ORR after adding 1 M CH_3OH in 0.1 M KOH solution. (b) Chronoamperometric response BA-TAP-Fe-800 and Pt/C for ORR.

Figure S12. (a) LSV curves for BA-TAP-Fe-700, BA-TAP-Fe-800 and BA-TAP-Fe-900 for OER. (b) LSV curves for BA-TAP-Fe-800 in 0.1 M KOH initially (black) and after 100 (red) CV sweeps for OER.

Figure S13. LSV curves of BA-TAP-Fe-800 and Pt/C for HER. LSV curves for BA-TAP-Fe-800 in 0.1 M KOH initially (black) and after 100 (red) CV sweeps vs. RHE in HER.

Figure S14. LSV curves of as-prepared and acid-leached BA-TAP-Fe-800 measured in 0.1 M KOH for ORR (a), OER (b) and HER (c). LSV curves of BA-TAP-Fe-800 measured in 0.5 M H_2SO_4 aqueous solution with and without adding 10 mM of NaSCN for ORR (d) and HER (e).

Experimental section

Chemicals. Barbituric acid (BA) was purchased from Sigma-Aldrich. 2, 4, 6-triaminopyrimidine (TAP), and $RuCl_3$ were obtained from J&K (China). Other chemicals and solvents were analytical grade, and purchased from Sinopharm Chemical Reagent Co., Ltd. (Shanghai, China) and used without further purification. Ultrapure water (18.2 MΩ cm^{-1}) was obtained from a Thermal Smart2 pure water purification system (USA).

Electrocatalyst synthesis. The BA-TAP was prepared by mixing BA (0.5 g) with TAP (0.5 g) in 40 mL of water. Then, the mixture was stirred for 4 hours using an automatic shaker. After that, the resultant pale yellow precipitate was collected by filtration, washed several times with water and dried at 60 ºC to produce the BA-TAP supramolecular aggregate (BA-TAP). The same procedure was used to synthesize BA-TAP-Fe. The BA-TAP and BA-TAP-Fe were calcined at desired temperature (700 - 900 ºC) with a heating rate of 5 ºC min^{-1} for 1h under N_2 atmosphere to produce BA-TAP-T and BA-TAP-Fe-T (T is the pyrolysis temperature). To explore the ORR active sites of the BA-TAP-Fe-800 catalyst, BA-TAP-Fe-800 was ball-milled with planetary ball-milling instrument (YXQM-0.4L, China) for 6 hours, leached in excessive concentrated HCl for 12 hours, and then washed with water to neutral, finally dried at 60 ºC (referred to as BA-TAP-Fe-800-L).

For comparison, BA-Fe-800 and TAP-Fe-800 were prepared by the same process as that for BA-TAP-Fe-800, except for without TAP or BA, respectively. BA+TAP-Fe-800 was prepared by ball milling of the mixture 0.5 g of BA, 0.5 g of TAP and 0.1 g $FeCl_3$ instead of the supramolecular approach, followed by the same heat treatment.

Synthesis of RuO_2 nanoparticles. RuO_2 nanoparticles were prepared according to previous report.[1] Briefly, $RuCl_3$ was dispersed in a 40 mL of solution consisted of 20 mL of methanol and 20 mL of water to result in a concentration of 50 mM for $RuCl_3$. The mixed solution was stirred at room temperature for 30 min. 2 M NaOH solution was then added into the mixed solution until the pH reached 7.0 and kept stirring for 30 min. The obtained black precipitate was obtained using a centrifuge, and then washed with water several times, followed by drying at 60 ºC and annealed at 500 ºC for 2h in air.

Electrochemical characterization. A RRDE-3A apparatus (ALS, Japan) in conjunction with a CHI 700E workstation (CHI, USA) was used to measure the electrocatalytic ORR, OER and HER activities. All the electrochemical measurements were carried out in a three-electrode cell. Ag/AgCl (saturated KCl) and platinum wire were used as reference and counter electrodes, respectively. The reliability of Ag/AgCl in our experimental conditions and the exclusion of the potential contamination of Pt were verified by the same results via exploring calomel electrode and carbon rods as the reference and counter electrode，respectively. The current density was normalized to the geometrical surface area, and the measured potentials vs. Ag/AgCl were converted to a reversible hydrogen electrode (RHE) scale according to the Nernst equation ($E_{RHE} = E_{Ag/Ag/Cl} + 0.059 \times pH + 0.197$). An RDE with a glassy carbon disk (3.0 mm diameter) and an RRDE with both a Pt ring and a glassy carbon disk (4.0 mm diameter) served as the substrate of the working electrodes in evaluating the electrocatalytic activity. Before use, the glassy carbon electrodes in RDE/RRDE were polished using aqueous alumina suspensions on felt polishing pads. The catalysts were suspended in ethanol with a concentration of 2 mg mL^{-1} and sonicated for 30 min to form homogeneous ink. For RDE measurements, 10 μL of catalyst ink was pipetted onto polished glassy carbon electrode to result in catalysts loading of 283 μg cm^{-2}. And then, the electrode was dried at RT and heated in air at 60 ^{o}C for 15 min. After that, 10 μL of Nafion solution (0.05 wt. %) was further pipetted onto the surface of the electrode. Then the electrode was dried again at RT and heated in air at 60 ^{o}C for 15 min. Before tests, N_2/O_2 flow was used through the electrolyte in the cell to achieve the N_2/O_2-saturated solution. The cyclic voltammetry (CV) profiles were obtained in N_2- or O_2-saturated 0.1 M KOH solution with a scan rate of 10 mV s^{-1}. RDE/RRDE tests for the ORR were measured in O_2-saturated 0.1 M KOH solution at different rotation rates with a scan rate of 10 mV s^{-1}. For stability and poisons tests of ORR, the chronoamperometric response at 0.4 V was recorded by RDE tests with a rotation rate of 1,600 rpm and followed by the introduction of 1 M methanol into 0.1 M KOH solution. Linear sweep voltammograms for the OER and HER were obtained using a RDE with a rotation rate of 1,600 rpm in KOH solution at a scan rate of 10 mV s^{-1}. For detection of peroxide species formed at the disc electrode, the potential of the Pt ring electrode in the RRDE measurements was set at 1.5 V. For comparison, the commercial Pt/C

(HiSPEC^{TM} 3000, 20 wt. % Pt on carbon black, Johnson Matthey) and RuO_2 nanoparticles were measured under the same experimental conditions. The catalysts loading is 197 μg cm^{-2} for Pt/C catalyst and 283μg cm^{-2} for the RuO_2 catalyst.

Hydrogen peroxide yields and the electron transfer number (n) were calculated using the equations below:[1-2]

$$HO_2^- = 200\frac{I_r / N}{I_d + I_r / N} \quad (1)$$

$$n = 4\frac{I_d}{I_d + I_r / N} \quad (2)$$

where I_d and I_r are the disk and ring currents, respectively. N is the ring collection efficiency and the measured N value was 0.42 in a solution of 5 mM $K_4Fe(CN)_6$ and 5 mM $K_3Fe(CN)_6$.

The Tafel slope was calculated according to Tafel equation as follows:

$$\eta = b\log j + a \quad (3)$$

where η denotes the overpotential, b denotes the Tafel slope, j denotes the current density.

Characterization. Fourier transform infrared spectra (FT-IR) were collected with a Nicolet 5700 FTIR spectrometer (Thermo, USA), equipped with an attenuated total reflection (ATR) setup. X-ray diffraction (XRD) patterns were recorded on a Rigaku (Smartlab 3 and Ultima IV, Japan) X-ray diffractometer equipped with graphite monochromatic Cu Kα radiation (λ = 1.54056 Å). The transmittance electron microscope (TEM) images were performed on JEM-2100 field emission electron microscopy at an acceleration voltage of 200 kV. The scanning electron microscope (SEM) images were measured on a Zeiss Ultra Plus scanning electron microscopy and Phenom ProX scanning electron microscope (The Netherlands). Energy dispersive X-ray (EDX) spectra were carried out on a Phenom ProX scanning electron microscope. X-ray photoelectron spectra (XPS) experiments were performed on a Theta probe (Thermo Fisher) with monochromated Al-Kα X-rays (hν = 1486.6 eV) as the excitation source. The binding energies obtained in the XPS analysis were corrected for specimen charging by reference C1s to 284.6 eV. Brunauer-Emmett-Teller (BET) surface area was calculated from N_2 adsorption-desorption isotherms collected at 77 K using a Nova 1200e (Quantachrome, USA). The Fe content was measured by inductively coupled plasma optical emission spectroscopy (ICP-OES, Leeman, USA).

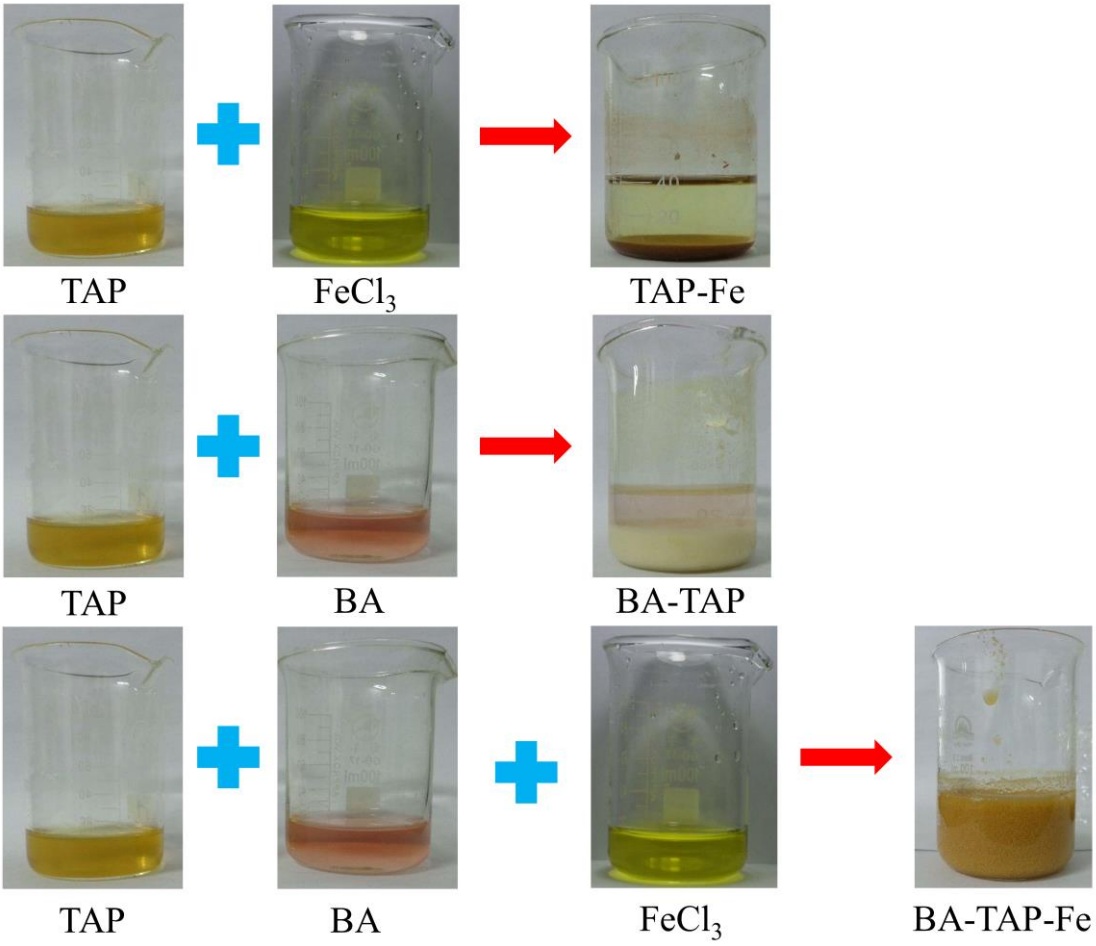

Figure S1. The preparation processes of (a) TAP-Fe, (b) BA-TAP, and (c) BA-TAP-Fe.

Figure S1a showed that the addition of $FeCl_3$ into an aqueous solution of melamine resulted in a dark brown precipitation, indicating $FeCl_3$ could be absorbed by TAP. Figure S1b showed that mixing TAP solution with BA solution resulted in a pale yellow precipitation, indicating the formation of BA-TAP supramolecular aggregate (BA-TAP). Figure S1c showed that mixing TAP solution with BA solution in the presence of $FeCl_3$ resulted in a deep yellow precipitation, indicating the formation of BA-TAP-Fe.

Figure S2. SEM image of BA-TAP.

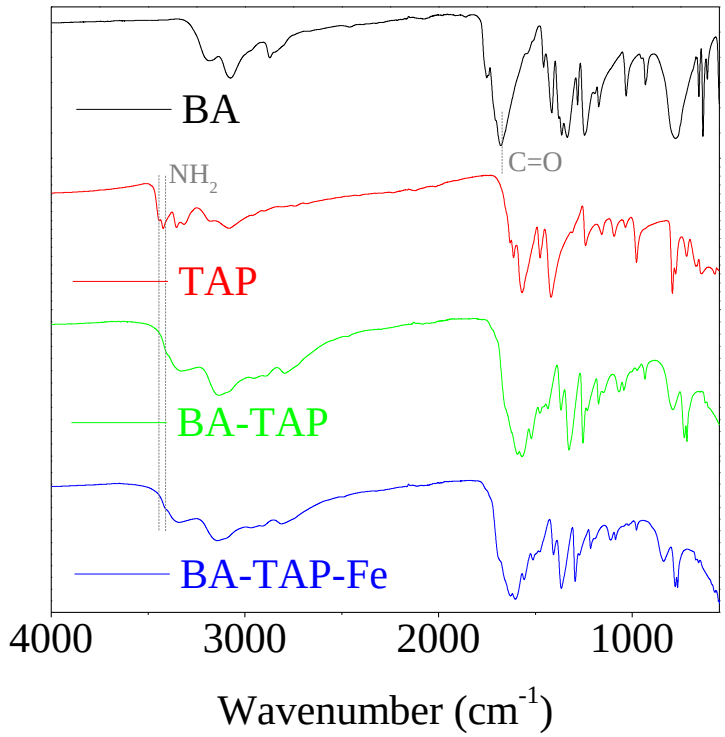

Figure S3. FT-IR spectra of the BA, TAP, BA-TAP and BA-TAP-Fe.

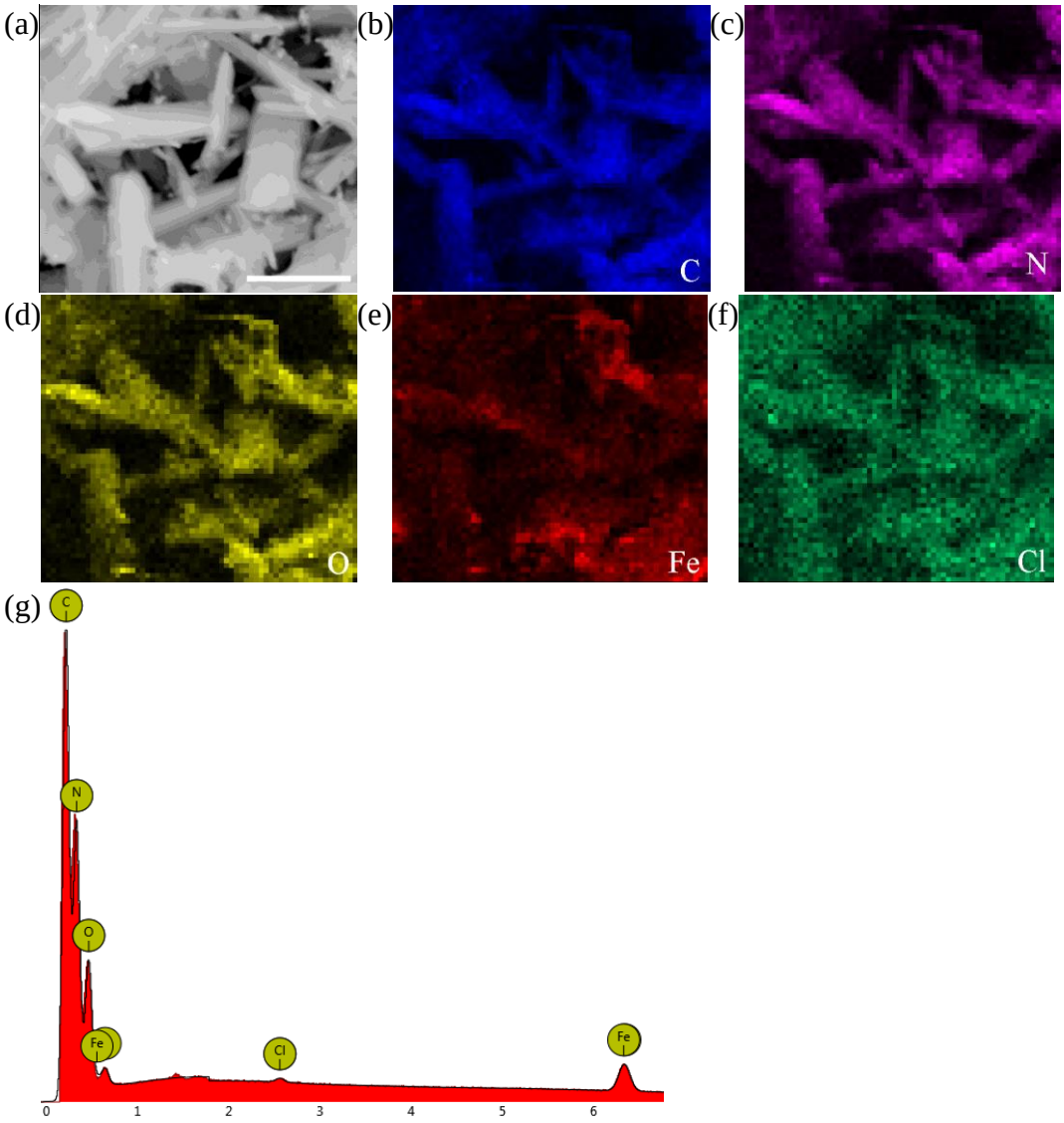

Figure S4. (a) SEM image of BA-TAP-Fe, and EDX elemental mapping images of (b) C, (c) N, (d) O, and (e) Fe, (f) Cl and (g) corresponding EDX spectrum. Scale bar: 5 μm.

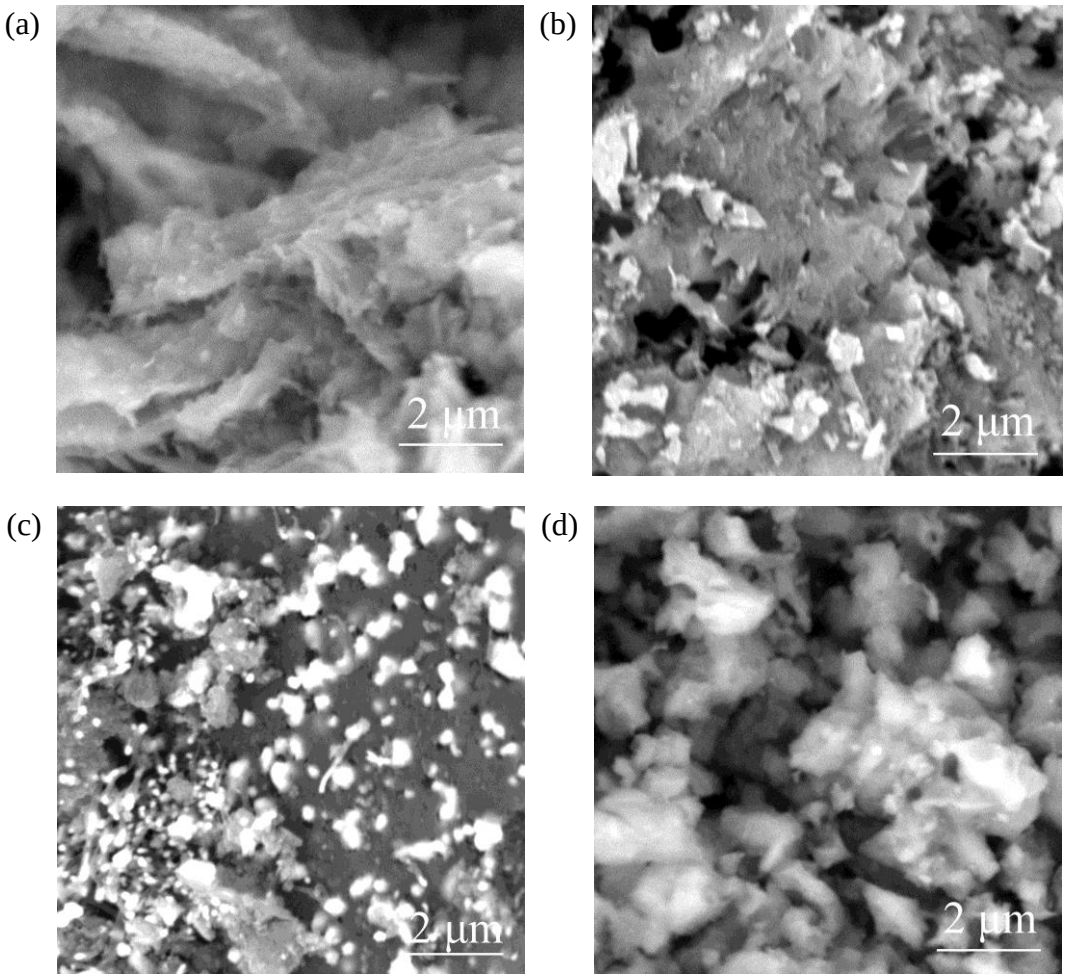

Figure S5. SEM images of BA-TAP-800 (a), BA-Fe-800 (b), TAP-Fe-800 (c) and BA+TAP+Fe-800 (d)

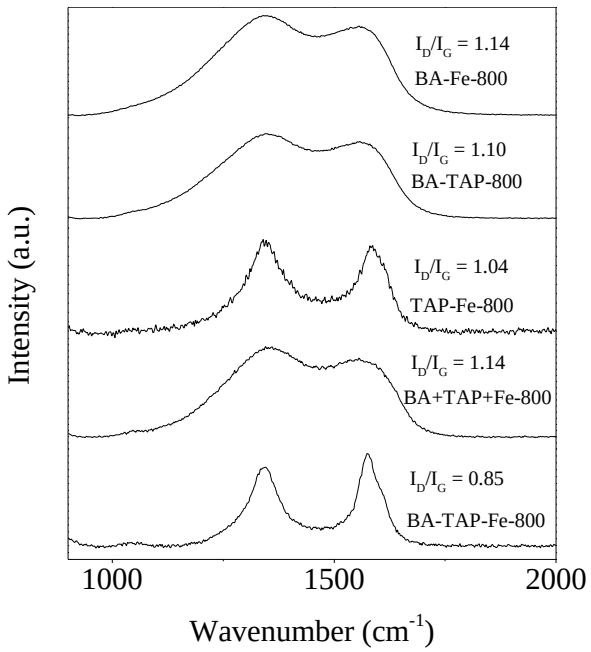

Figure S6. Raman spectra of BA-Fe-800, BA-TAP-800, TAP-Fe-800, BA+TAP+Fe-800, and BA-TAP-Fe-800.

As shown in Figure S6, the Raman spectra showed BA-TAP-Fe-800 had a relatively lower intensity ratio of D-band to G-band (I_D/I_G) in comparison with control samples without supramolecular preorganization, implying the higher degree of graphitization. According to previous reports on in situ growth of CNTs,[3] it can be inferred that the $FeCl_3$ precursor would be reduced by carbon to metallic iron atom during pyrolysis. On one hand, Fe atoms would interact with nitrogen atoms to generate the Fe-N_x species. On the other hand, the excessive Fe would aggregate into Fe nanoparticles, which could further interact with carbon to form FeC_3 nanoparticles and catalytically graphitize carbon to form the protected carbon-encapsulated nanoparticles, thus promoting the degree of graphitization in the heat treatment process.

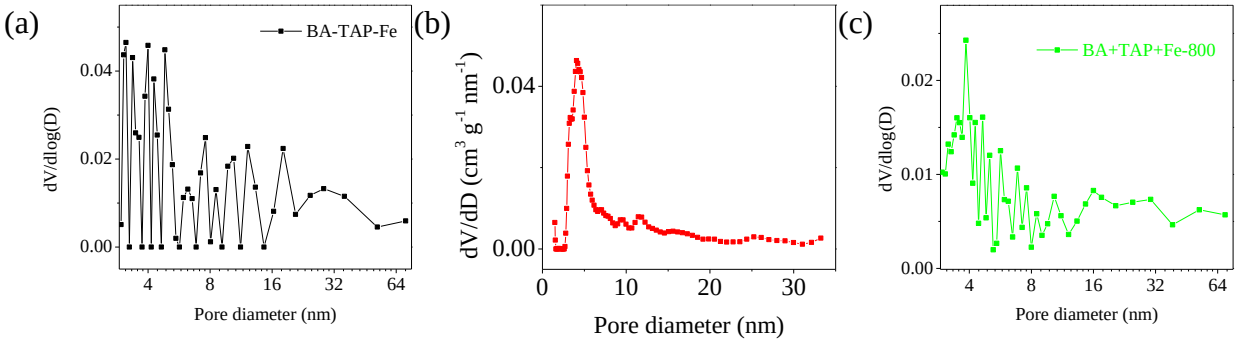

Figure S7. Pore size distribution of BA-TAP-Fe (a), BA-TAP-Fe-800 (b) and BA+TAP+Fe-800 (c, prepared by ball-mill mixing of BA, TAP and $FeCl_3$ and the identical pyrolysis process).

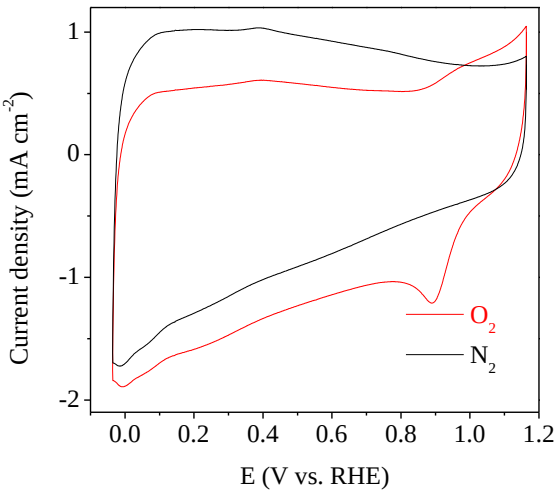

Figure S8. CV profiles of BA-TAP-Fe-800 in O_2-saturated and N_2-saturated 0.1 M KOH solution at a scan rate of 10 mV s^{-1}.

The catalytic activity for ORR of the as-prepared BA-TAP-Fe-800 was first assessed by cyclic voltammetry (CV). As shown in Figure S8, a well-defined cathodic peak was clearly observed at 0.89 V in O_2-saturated 0.1 M KOH electrolyte, but not in N_2-saturated electrolyte, confirming the electrocatalytic activity for ORR.

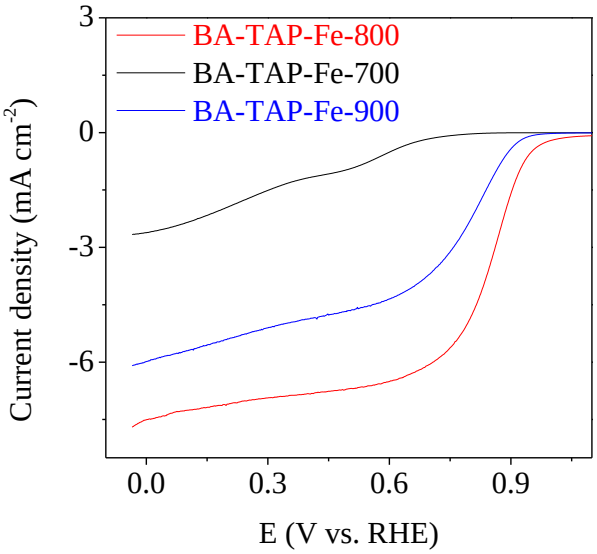

Figure S9. LSV curves of BA-TAP-Fe-800, BA-TAP-Fe-700 and BA-TAP-Fe-900 in O_2-saturated 0.1 M KOH solution at rotating disk electrodes. Rotation rate: 1600 rpm, scanning rate: 10 mV s^{-1}.

The ORR activity of catalysts prepared at different temperature were further studied using rotating disk electrode (RDE) measurements. As shown in Figure S9, the highest onset potential and largest cathodic current density was harvested by BA-TAP-Fe-800, because a balance of porosity, degree of graphitization, surface area, and type and density of active site could be optimized at 800 ^oC (see Table S1 and more discussion).[4]

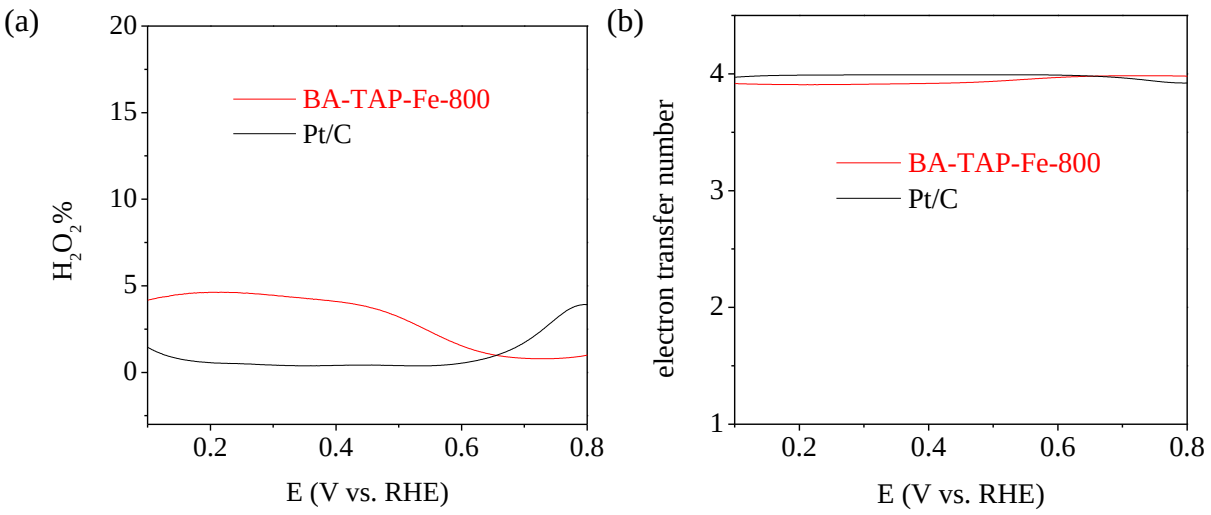

Figure S10. (a) Hydrogen peroxide yield and (b) corresponding electron transfer number of BA-TAP-Fe-800 and Pt/C for ORR.

The measured H_2O_2 yield was below ~5%, over the potential range of 0.1 to 0.8 V, giving an electron transfer number of ~3.90 (Figure S10b), and confirming that catalytic ORR by BA-TAP-Fe-800 was mainly through a 4e pathway (Figure S10).

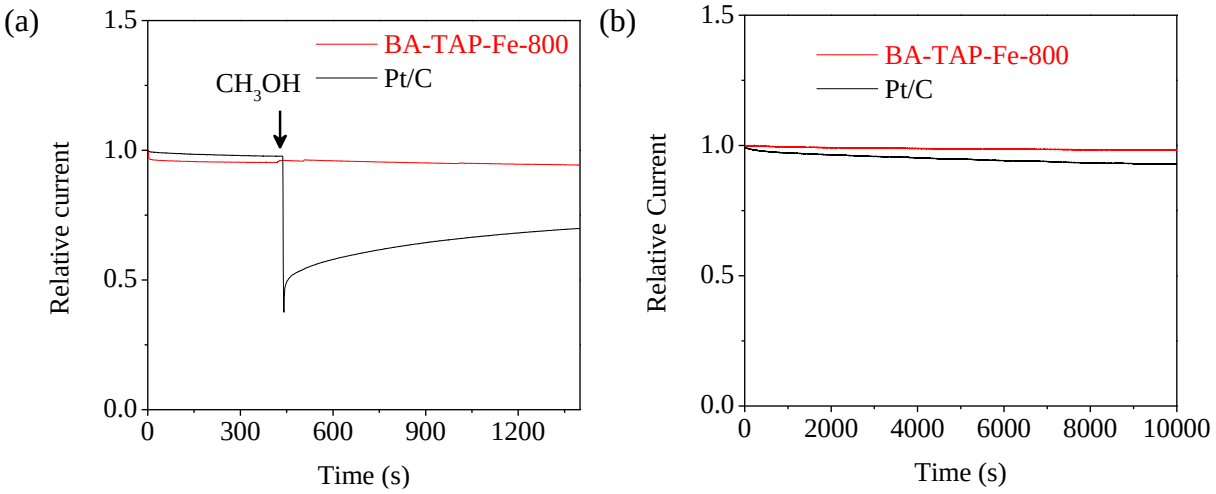

Figure S11. (a) Chronoamperometric response of BA-TAP-Fe-800 and Pt/C at 0.5 V for ORR after adding 1 M CH_3OH in 0.1 M KOH solution. (b) Chronoamperometric response BA-TAP-Fe-800 and Pt/C at 0.5 V for ORR.

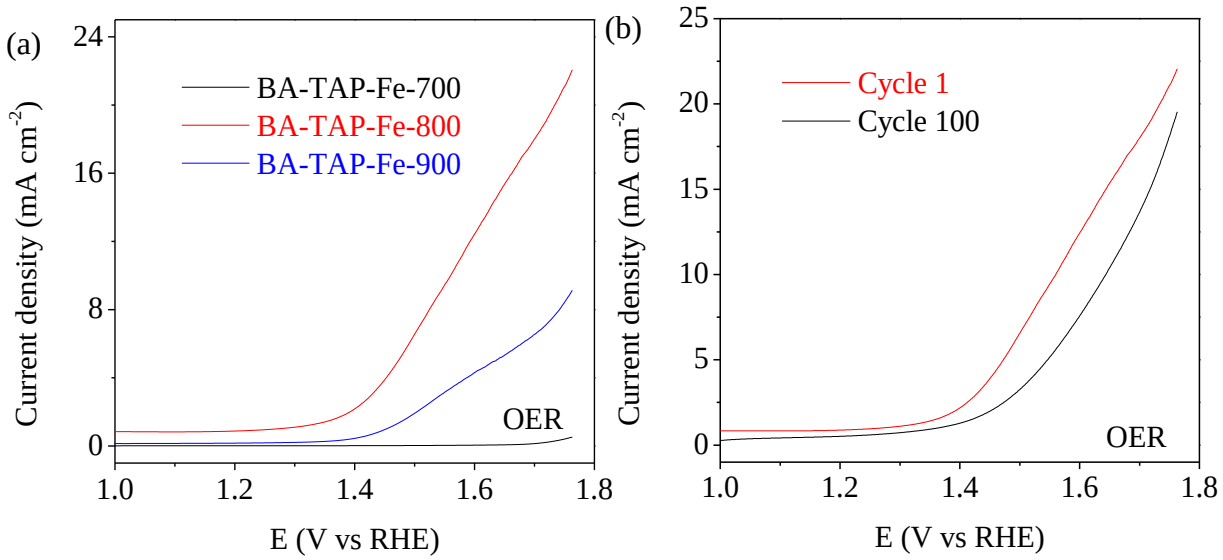

Figure S12. (a) LSV curves for BA-TAP-Fe-700, BA-TAP-Fe-800 and BA-TAP-Fe-900 for OER. (b) LSV curves for BA-TAP-Fe-800 in 0.1 M KOH initially (black) and after 100 (red) CV sweeps for OER.

The OER activity of different catalysts prepared at 700, 800 and 900 ^{o}C is given in Figure S12a and further compared to control samples without supramolecular approach such as BA+TAP-Fe-800, BA-TAP-800, TAP-Fe-800, and BA-$FeCl_3$-800 (Figure 5). Interestingly, BA-TAP-Fe-800 exhibited the best OER activity in the onset potentials and potential for current density of 10 mA cm^{-2}.

The stability of the materials under catalytic conditions was also determined by collecting polarization curves between 1 and 1.7 V (vs. RHE) over 100 cycles. Upon cycling, an increase in the potential for current density of 10 mA cm^{-2} was observed from 1.55 to 1.64 V presumably due to partial surface oxidation of Fe or carbon corrosion (Figure S12b), which was usually observed in other metal-containing carbon catalyst.[5] These results demonstrated that BA-TAP-Fe-800 was a remarkably efficient electrocatalyst for OER.

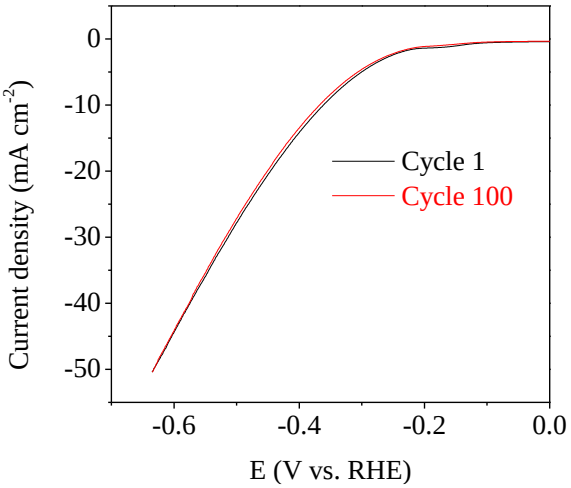

Figure S13. LSV curves of BA-TAP-Fe-800 and Pt/C for HER. LSV curves for BA-TAP-Fe-800 in 0.1 M KOH initially (black) and after 100 (red) CV sweeps vs. RHE in HER.

As shown in Figure S13, the BA-TAP-Fe-800 showed almost no change after continued cycling (100 cycles), clearly indicating the remarkable operation stability.

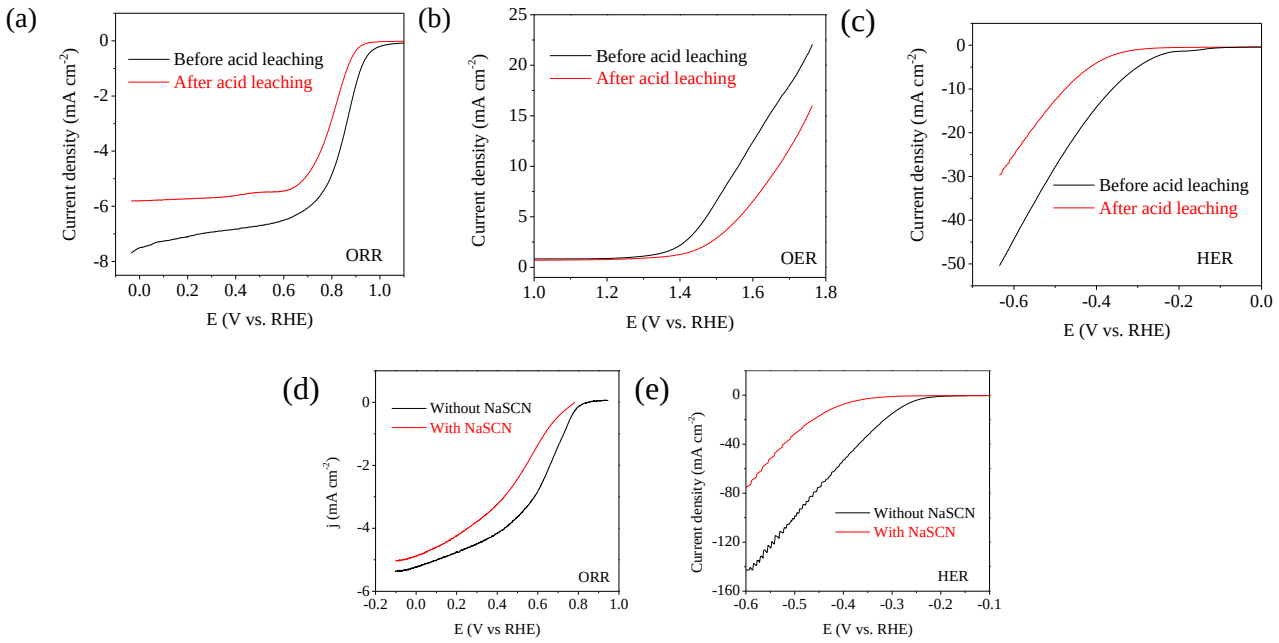

Figure S14. LSV curves of as-prepared and acid-leached BA-TAP-Fe-800 measured in 0.1 M KOH for ORR (a), OER (b) and HER (c). LSV curves of BA-TAP-Fe-800 measured in 0.5 M H_2SO_4 aqueous solution with and without adding 10 mM of NaSCN for ORR (d) and HER (e).

To further understand the nature of catalytic active sites, another two control experiments were carried out. (1) The catalyst BA-TAP-Fe-800 was ball-milled to destroy the protective carbon shells around Fe/Fe_3C nanoparticles,[6] and then leached in concentrated HCl (referred as BA-TAP-Fe-800-L). ICP-OES showed that the Fe content largely reduced from 19.8 wt. to % 2.3 wt., demonstrating Fe/Fe_3C nanoparticles were largely removed after leaching. As a result, BA-TAP-Fe-800-L showed apparently degraded ORR, OER and HER activity (Figure S14a-c). As shown in Figure S14a, ORR activity of BA-TAP-Fe-800-L showed a significant deterioration that the half wave potential negatively shifted by about 100 mV and the diffusion-limiting current remarkably decreased compared to BA-TAP-Fe-800. As shown in Figure S14b, the polarization curve of OER showed the potential for current density of 10 mA cm^{-2} increased from 1.56 to 1.70 V after acid leaching. The polarization curve of HER potential for current density of 10 mA cm^{-2} also increased from -0.33 to -0.48 V (Figure S14c). These results indicated that Fe/Fe_3C nanoparticles played an important role in the high catalytic activity in BA-TAP-Fe-800. (2) Considering potential reaction between SCN^- ion and KOH,[3a, 7] we measured the ORR and HER activity of BA-TAP-Fe-800 in 0.5 M H_2SO_4 with 0.01 M NaSCN. It can be seen in that the half wave potential of BA-TAP-Fe-800 decreased significantly by about 160 mV after the addition of 0.01 M NaSCN (Figure S14d). The remarkably depression of catalytic activity for HER was also observed (Figure S114e). The potential for current density of 10 mA cm^{-2} also increased by 140 mV. It should be noted that the poison test of OER by SCN^- ion was not investigated because SCN^- may be oxidized. The remarkably depression of catalytic activity was observed (Figure S14e-d), which confirmed that Fe-N_x sites should be responsible for the ORR and HER activity of BA-TAP-Fe-800, attributing to the blocking of Fe-N_x active sites by SCN^- in catalyzing ORR and HER.[3a, 7-8].Therefore, these two control experiments strongly verified that the coexistence of Fe/Fe_3C nanoparticles and Fe-N_x active sites were essential to the outstanding ORR, OER and HER

electrocatalytic performances for BA-TAP-Fe-800.

Therefore, the superior electrocatalytic activities of BA-TAP-Fe-800 may mainly be attributed to the following factors: (1) the BA-TAP-Fe-800 exhibited the desired hierarchical that derived from the supramolecular precursors and high degree of graphitization, which were favorable for active site exposure and rapid electrocatalysis-relevant species transport. (2) The intimate contact between crystalline Fe/FeC_3 nanoparticles and highly graphitic carbon shell was supposed to efficiently improve catalytic activities in the BA-TAP-Fe-800 electrocatalytic system. The outer protective graphitic layers could sustain the stability of the carbide nanoparticles, and the inner Fe/Fe_3C nanoparticles, despite not indirect contact with the electrolyte, could activate the outer surface of the surrounding graphitic layers towards the electrocatalysis.[3a, 3b, 6b] (3) $Fe\text{-}N_x$ configuration in the catalyst improved the catalytic activity. (4) A synergetic catalytic effect may be generated between $Fe\text{-}N_x$ and Fe/FeC_3.

Table S1. Summary of typical bi/tri-functional electrocatalysts reported in recent two years

Catalyst	Catalyst loading (mg cm^{-2})	E_{ORR}/V Onset potential	E_{OER}/V 10 mA cm^{-2}	ΔE/V (E_{OER}-E_{ORR})
Co@Co_3O_4/N-doped carbon[9]	0.21	0.80	1.65	0.85
N, P co-doping carbon[1]	0.15	0.94	>1.7	>0.74
Fe–N–C/NiFe-LDH[10]	0.2	0.92	1.54	0.62
N-Carbon nanotube frameworks[11]	0.2	0.97	1.60	0.63
$ZnCo_2O_4$/N-CNT[12]	0.2	0.95	1.65	0.7
P-g-C_3N_4/carbon-fiber paper[13]	0.2	0.94	1.63	0.69
Co_3O_4-carbon porous nanowire arrays[14]	0.2	0.91	1.52	0.61
Co/N-doped carbon[15]	0.3	0.95	1.69	0.74
Co/N-CNTs[16]	0.2	0.96	1.62	0.66
NiCo-porous fibrous carbon aerogels[17]	0.13	0.92	1.63	0.71
N, P, and F tri-doped Graphene[18]	0.5	0.9	1.8	0.9
S/N/Fe-doped carbon[19]	0.8	0.93	1.78	0.85
Pt/C-BSCF[20]	0.464	0.90	1.61	0.71
N/Co-doped carbon[21]	0.714	0.94	1.66	0.72
Pt/C (This work)	0.197	0.95	1.85	0.9
BA-TAP-Fe-800 (This work)	0.283	1.02	1.55	0.53
Catalyst	Catalyst loading (mg cm^{-2})	E_{HER}/V 10 mA cm^{-2}	E_{OER}/V 10 mA cm^{-2}	ΔE/V (E_{OER}-E_{HER})

Pt/C (This work)	0.197	-0.1	1.85	1.95
$CoO/CoSe_2$[22]	2.0	-0.34	1.74	2.08
CoO_x@ N-doped carbon[5a]	0.12	-0.23	1.62	1.85
Mn_1Ni_1[23]	0.2	-0.36	1.65	2.01
NiSe nanowire/nickel foam[24]	2.8	-0.1	1.63	1.73
N, P, and F tri-doped Graphene[18]	0.5	-0.52	1.8	2.32
N/Co-doped carbon[21]	0.714	-0.22	1.66	1.88
BA-TAP-Fe-800 (This work)	0.283	-0.33	1.55	1.88

Table S1 shows the electrocatalytic activity of BA-TAP-Fe-800, comparing to those of reported bi/tri-functional electrocatalyst in recent two years, in terms of the difference of OER and ORR metrics ($\Delta E = E_{j = 10} - E_{onset}$) and HER and OER metrics ($\Delta E = E_{OER/j = 10} - E_{HER/j = 10}$). In general, from a practical point of view, the smaller ΔE is, the closer the catalyst is to an ideal reversible oxygen electrode and overall water splitting. BA-TAP-Fe-800 exhibits a ΔE value of 0.53 V and 1.88 V, lower than that of the recently reported highly active bifunctional electrocatalyst.

Table S2. Summary of various electrocatalysts for ORR.

Catalysts	Catalyst loading (mg cm^{-2})	Onset potential (V)	Half-wave potential (V)	Reference
PANI-Fe-C	0.6	0.93	0.81	Science 2011, 332, 443
N and P co-doped nanocarbon	0.15	0.94	0.85	Nat. Nanotech. 2015, 10, 444
N-CNT frameworks	0.2	0.97	0.87	Nature Energy 2016, 1, 15006.
CNT/graphene hybrid	0.49	0.89	0.76	Nat. Nanotech. 2012, 7, 394
Co_3O_4/rmGO	0.17	0.88	0.79	Nat. Mater. 2011, 10, 780
Co_3O_4/N-rmGO	0.17	0.88	0.83	Nat. Mater. 2011, 10, 780
Mesoporous N-doped carbon	0.1	0.978	0.85	Nat. Commun. 2014, 5, 5973
NCNT/carbon nanoparticle	1	1.08	0.93	Nat. Commun. 2013, 4, 1922
Co/Co_3O_4@Carbon	0.21	0.92	0.83	Angew. Chem. Int. Ed. 2016, 55, 4087
Fe@C-FeNC	0.70	N/A	0.899	J. Am. Chem. Soc. 2016, 138, 3570
Carbon nanotube /Fe_3C hybrids	1.2	N/A	0.861	J. Am. Chem. Soc. 2015, 137, 1436
FeNx/C catalyst	0.6	0.94	0.82	J. Am. Chem. Soc. 2014, 136, 10882
CNTs/carbon hybrid	0.6	0.92	0.82	Angew. Chem. Int. Ed. 2014, 53, 4102
N-doped graphene/metals	0.6	0.94	N/A	Angew. Chem. Int. Ed. 2014, 53, 1570
Fe−N/C-800	0.1	0.92	0.80	J. Am. Chem. Soc. 2014, 136, 1102
Graphene-MOF composite	0.16	0.91	N/A	J. Am. Chem. Soc. 2012, 134, 6707
MOF-derived carbons	0.2	0.9	N/A	Angew. Chem. Int. Ed. 2014, 53, 2433
ZIF-derived porous carbons	0.4	0.9	0.76	Adv. Mater. 2014, 26, 1093
ZIF-derived porous carbon/graphene	0.2	0.95	N/A	Angew. Chem. Int. Ed. 2014, 53, 14235
P-doped ordered mesoporous carbon	0.3	0.92	0.82	Angew. Chem. Int. Ed. 2015, 54, 9230
Sulphur-doped graphene	0.08	0.88	0.66	Angew. Chem. Int. Ed. 2015, 54, 1888
Fe_3C/Fe-N-C	0.3	0.98	N/A	Angew. Chem. Int. Ed. 2016, 128, 1377
Fe-N-doped carbon nanofibers	0.6	0.944	0.824	Angew. Chem. 2015, 127, 8297
Nitro Lignin derived Nitrogen Doped Carbon	0.29	N/A	0.85	ACS Nano, 2016, 10, 4364
BA-TAP-Fe-800	0.283	1.02	0.85	This work

Table S3. Summary of various electrocatalysts for OER.

Catalysts	Loading (mg cm^{-2})	Onset potential (V)	Potential (V) @10 mA cm^{-2}	References
Carbon nanotube frameworks	0.2	N/A	1.60 V	Nature Energy 2016, 1, 15006
Co nanoparticles/C hybrid	0.2	N/A	1.62	J. Am. Chem. Soc. 2015, 137, 7071
CoMnP nanoparticles	0.284	N/A	1.56	J. Am. Chem. Soc. 2016, 138, 4006
g-C_3N_4 Nanosheets/carbon nanotubes	0.204	1.53	1.60	Angew. Chem. Int. Ed. 2014, 53, 7281
g-C_3N_4 Nanosheets/Graphene	0.497	1.544	1.769	ChemSusChem 2014, 7, 2125
CoO_x@CN	0.42	N/A	1.60	J. Am. Chem. Soc. 2015, 137, 2688
N/Co-doped MOF derived carbon/NRGO	0.36	N/A	1.66	Adv. Funct. Mater. 2015, 25, 872
phosphorus-doped g-C_3N_4/carbon fiber	0.20	1.53	1.63	Angew. Chem. Int. Ed. 2015, 54, 464
Carbon Nitride/Titanium Carbide Nanosheet hybrid	1.4	1.44	1.54	Angew. Chem. Int. Ed. 2016, 55, 1138
NiSe Nanowire Film	2.8	N/A	1.50	Angew. Chem. Int. Ed. 2015, 54, 9351
N-doped carbons	0.2	N/A	1.61	Nat. Commun. 2013, 4, 2390
BA-TAP-Fe-800	0.283	1.36	1.55	This work

Reference:

1. J. Zhang, Z. Zhao, Z. Xia and L. Dai, *Nat. Nanotech.*, 2015, **10**, 444-452.
2. T. Y. Ma, J. Ran, S. Dai, M. Jaroniec and S. Z. Qiao, *Angewandte Chemie*, 2015, **127**, 4729-4733.
3. (a) W. Jiang, L. Gu, L. Li, Y. Zhang, X. Zhang, L. Zhang, J. Wang, J. Hu, Z. Wei and L. Wan, *J. Am. Chem. Soc.*, 2016, **138**, 3570-3578; (b) Z. Wu, X. Xu, B. Hu, H. Liang, Y. Lin, L. Chen and S. Yu, *Angew. Chem. Int. Ed.*, 2015, **54**, 8179-8183; (c) W. Ding, L. Li, K. Xiong, Y. Wang, W. Li, Y. Nie, S. Chen, X. Qi and Z. Wei, *J. Am. Chem. Soc.*, 2015, **137**, 5414-5420.
4. F. He, X. Chen, Y. Shen, Y. Li, A. Liu, S. Liu, T. Mori and Y. Zhang, *J. Mater. Chem. A*, 2016, **4**, 6630-6638.
5. (a) H. Jin, J. Wang, D. Su, Z. Wei, Z. Pang and Y. Wang, *J. Am. Chem. Soc.*, 2015, **137**, 2688-2694; (b) L. Wu, Q. Li, C. H. Wu, H. Zhu, A. Mendoza-Garcia, B. Shen, J. Guo and S. Sun, *J. Am. Chem. Soc.*, 2015, **137**, 7071-7074; (c)

D. Li, H. Baydoun, C. N. Verani and S. L. Brock, *J. Am. Chem. Soc.*, 2016, **138**, 4006-4009; (d) J. Chen, J. B. Siegel, T. Matsuura and A. G. Stefanopoulou, *J. Electrochem. Soc.*, 2011, **158**, B1164.

6. (a) U. I. Kramm, I. Herrmann-Geppert, J. Behrends, K. Lips, S. Fiechter and P. Bogdanoff, *J. Am. Chem. Soc.*, 2016, **138**, 635-640; (b) Y. Hu, J. O. Jensen, W. Zhang, L. N. Cleemann, W. Xing, N. J. Bjerrum and Q. Li, *Angew. Chem. Int. Ed.*, 2014, **53**, 3675-3679.
7. Q. Wang, Z. Y. Zhou, Y. J. Lai, Y. You, J. G. Liu, X. L. Wu, E. Terefe, C. Chen, L. Song, M. Rauf, N. Tian and S. G. Sun, *J. Am. Chem. Soc.*, 2014, **136**, 10882-10885.
8. H.-W. Liang, S. Brüller, R. Dong, J. Zhang, X. Feng and K. Müllen, *Nat. Commun.*, 2015, **6**, 7992.
9. A. Aijaz, J. Masa, C. Rösler, W. Xia, P. Weide, A. J. R. Botz, R. A. Fischer, W. Schuhmann and M. Muhler, *Angew. Chem. Int. Ed.*, 2016, **55**, 4087-4091.
10. S. Dresp, F. Luo, R. Schmack, S. Kühl, M. Gliech and P. Strasser, *Energy Environ. Sci.*, 2016, **9**, 2020-2024.
11. B. Y. Xia, Y. Yan, N. Li, H. B. Wu, X. W. Lou and X. Wang, *Nature Energy*, 2016, **1**, 15006.
12. Z.-Q. Liu, H. Cheng, N. Li, T. Y. Ma and Y.-Z. Su, *Adv. Mater.*, 2016, **28**, 3777-3784.
13. T. Y. Ma, J. Ran, S. Dai, M. Jaroniec and S. Z. Qiao, *Angew. Chem. Int. Ed.*, 2015, **127**, 4729-4733.
14. T. Y. Ma, S. Dai, M. Jaroniec and S. Z. Qiao, *J. Am. Chem. Soc.*, 2014, **136**, 13925-13931.
15. J. Wei, Y. Liang, Y. Hu, B. Kong, J. Zhang, Q. Gu, Y. Tong, X. Wang, S. P. Jiang and H. Wang, *Angew. Chem. Int. Ed.*, 2016, **55**, 12470-12474.
16. Y. Liu, H. Jiang, Y. Zhu, X. Yang and C. Li, *J. Mater. Chem. A*, 2016, **4**, 1694-1701.
17. G. Fu, Y. Chen, Z. Cui, Y. Li, W. Zhou, S. Xin, Y. Tang and J. B. Goodenough, *Nano Lett.*, 2016, **16**, 6516-6522.
18. J. Zhang and L. Dai, *Angew. Chem. Int. Ed.*, 2016, **55**, 13296-13300.
19. N. Ranjbar Sahraie, J. P. Paraknowitsch, C. Göbel, A. Thomas and P. Strasser, *J. Am. Chem. Soc.*, 2014, **136**, 14486-14497.
20. Y. Zhu, C. Su, X. Xu, W. Zhou, R. Ran and Z. Shao, *Chem. Eur. J.*, 2014, **20**, 15533-15542.
21. Y. Hou, Z. Wen, S. Cui, S. Ci, S. Mao and J. Chen, *Adv. Funct. Mater.*, 2015, **25**, 872-882.
22. K. Li, J. Zhang, R. Wu, Y. Yu and B. Zhang, *Advanced Science*, 2016, **3**, 1500426.
23. M. Ledendecker, G. Clavel, M. Antonietti and M. Shalom, *Adv. Funct. Mater.*, 2015, **25**, 393-399.
24. C. Tang, N. Cheng, Z. Pu, W. Xing and X. Sun, *Angew. Chem. Int. Ed.*, 2015, **54**, 9351-9355.